



LAWRENCE  
LIVERMORE  
NATIONAL  
LABORATORY

# Real-time observation of nanosecond liquid-phase assembly of nickel nanoparticles via pulsed-laser heating

J. T. McKeown, N. A. Roberts, J. D. Fowlkes, T. LaGrange, B. W. Reed, G. H. Campbell, P. D. Rack

January 12, 2012

Langmuir

## **Disclaimer**

---

This document was prepared as an account of work sponsored by an agency of the United States government. Neither the United States government nor Lawrence Livermore National Security, LLC, nor any of their employees makes any warranty, expressed or implied, or assumes any legal liability or responsibility for the accuracy, completeness, or usefulness of any information, apparatus, product, or process disclosed, or represents that its use would not infringe privately owned rights. Reference herein to any specific commercial product, process, or service by trade name, trademark, manufacturer, or otherwise does not necessarily constitute or imply its endorsement, recommendation, or favoring by the United States government or Lawrence Livermore National Security, LLC. The views and opinions of authors expressed herein do not necessarily state or reflect those of the United States government or Lawrence Livermore National Security, LLC, and shall not be used for advertising or product endorsement purposes.

# Real-time observation of nanosecond liquid-phase assembly of nickel nanoparticles via pulsed-laser heating

*Joseph T. McKeown<sup>1</sup>, Nicholas A. Roberts<sup>2</sup>, Jason D. Fowlkes<sup>3</sup>, Thomas LaGrange<sup>1</sup>,  
Bryan W. Reed<sup>1</sup>, Geoffrey H. Campbell<sup>1</sup>, and Philip D. Rack<sup>2,3,\*</sup>*

<sup>1</sup> Condensed Matter and Materials Division, Lawrence Livermore National Laboratory,  
Livermore, CA 94550, USA

<sup>2</sup> Materials Science and Engineering Department, The University of Tennessee, Knoxville, TN  
37996, USA

<sup>3</sup> Center for Nanophase Materials Science, Oak Ridge National Laboratory, Oak Ridge, TN  
37831, USA

\* Corresponding author: [prack@utk.edu](mailto:prack@utk.edu)

## Abstract

Using the dynamic transmission electron microscope (DTEM), the dewetting of thin nickel films was monitored at nanometer spatial and nanosecond timescales to provide insight into the liquid-phase assembly dynamics. Correlated time and length scales indicate that a spinodal instability drives the assembly process. Measured lifetimes of the liquid metal agree with finite-element simulations of the laser-irradiated film. These results can be used to design improved synthesis and assembly routes toward achieving advanced functional nanomaterials and devices.

## Keywords

assembly dynamics, dynamic transmission electron microscopy, pulsed-laser heating, thin-film dewetting

## Letter

The synthesis and organization of functional nanomaterials via bottom-up self- and directed assembly represents a critical challenge for the future of nanoscience. Generating arrays of nanoparticles with controlled size and spatial distributions is key to this challenge, and processes that exploit morphological instabilities offer the potential to attain these fine-scale spatially correlated structures. There has been long-standing interest in the capillarity and surface tension effects on morphological evolution in various materials systems, dating back to the work of Plateau<sup>1</sup> and Rayleigh<sup>2</sup>. Recently, pulsed-laser-induced dewetting of two-dimensional films<sup>3-9</sup>, one-dimensional lines and rings<sup>10-13</sup>, and lithographically patterned nanostructures<sup>14,15</sup> has demonstrated that understanding and controlling thin-film and Rayleigh-Plateau instabilities improves the ability to create organized metallic nanoparticle ensembles. Assembled particles have also been shown to “jump” or eject from one substrate and transfer to another depending on the energetics and dynamics of various laser-melted nanostructures<sup>16-18</sup>. Heretofore, the nanosecond liquid-phase dynamics have been inferred by *ex-situ* observations of the re-solidified metal quenched after different liquid lifetimes<sup>19</sup>. To gain further insight into the assembly dynamics, we present initial results for the nanoscale (time and length) observation of the dewetting of a 10-nm-thick nickel film that has been pulsed-laser melted *in-situ* using the dynamic transmission electron microscope (DTEM)<sup>20-27</sup>.

Liquid nickel has an equilibrium contact angle with silicon nitride of  $\sim 120^\circ$ <sup>28</sup> (consistent with a  $104 \pm 10^\circ$  angle measured via tilted SEM images of resultant dewet nanoparticles—see Supporting Information), and therefore nickel thin films can be expected to dewet silicon nitride substrates upon heating. Figure 1 shows conventional bright-field TEM images of a) an as-deposited Ni film and b) the Ni film after pulsed-laser-induced melting, which shows dewetting and nanoparticle formation near the edge of the laser spot (the center of the laser spot is in the direction of the lower-left corner of the image). The change in the dewetting pattern from the lower-left corner to the upper-right corner of Figure 1b) demonstrates the change in radial laser fluence due to a Gaussian beam profile, resulting in a radial liquid time-temperature profile. Higher-magnification images are shown for c) the saturated nanoparticle morphology and d) the earlier-stage interconnected rivulet morphology. Inset in Figure 1c) is an image of a single

nanoparticle that shows twinning, consistent with rapid solidification. It is also evident from the contrast of the particles that they are polycrystalline.

Figure 2 shows dynamic TEM images of a) an initial film region prior to laser exposure and after time delays of b) 15 ns and c) 20 ns, respectively. Each image represents a different area of the deposited film that was laser treated and imaged under identical experimental conditions but at different time delays. The lower left corner of the images is approximately the laser center and, as described in the Methods section, the laser spot has a Gaussian profile and thus the radial profile of each image also contains thermal and temporal information. Figure 2d) shows an image taken long after a laser pulse to show the resultant nanoparticle structure in the same field of view. The images in Figure 2 were filtered to remove noise and irrelevant intensity variations using a 3x3 median filter followed by a local brightness and contrast equalization filter using a Gaussian kernel with an rms width of 33 pixels in the x- and y-directions. The raw images are provided in the Supporting Information.

Dynamic selected-area diffraction (SAD) patterns were recorded as a function of time to complement the dynamic imaging and estimate the nickel liquid lifetime. Figure 3a) shows a series of SAD patterns taken at various times relative to the specimen pump laser's interaction with the specimen (including as-deposited and post-laser-pulse diffraction patterns using a long exposure time). The simulated diffraction pattern for polycrystalline nickel is included in the long-exposure as-deposited diffraction pattern. The conventional diffraction pattern from the as-deposited film shows broad diffraction rings due to finite crystal-size effects, indicating that the film is nanocrystalline, which can also be observed in the bright-field image of Figure 1a). After the film has dewet, the diffraction pattern shows spotted rings due to the larger-grain polycrystalline morphology. While there appears to be a slight  $\{111\}$  preferred orientation in the as-deposited thin film<sup>29-31</sup>, there is no preferred orientation or texture seen in the dewet film.

The time labeled on each diffraction pattern is the delay between the arrival times of the peaks of the specimen pump laser pulse and the electron probe pulse at the specimen. Both pulse widths are  $\sim 15$  ns, and thus each exposure (time-resolved diffraction pattern or image) is a time-averaged snapshot over 15 ns. Thus for  $|t| < 10$  ns, the two pulses overlap significantly such that

the sample is being rapidly heated during the exposure. This accounts for the observed heating effects at negative times.

Inspection of the time-resolved diffraction patterns in Figure 3a) reveals changes in the structure of the nickel film indicative of melting and re-solidification<sup>32</sup>. There is a noticeable change in the short-range order at times as short as the first ten nanoseconds (-5 ns diffraction pattern) after interaction of the pump laser with the specimen, evidenced by a broadening of the {111} diffraction ring and a disappearance of higher-order diffraction rings. Figure 3b) shows radially averaged patterns of the experimental data in Figure 3a) that more clearly illustrate the dynamics of the laser melting process. Following the progression of the peaks centered about the {111} and {200} lattice spacings, a broadening of both peaks is observed beginning at around -5 ns. The {111} peak continues to broaden and become diffuse with time, while the intensity of the {200} peak decreases with time, disappearing altogether by 5 ns, at which time the diffraction pattern consists of a single diffuse diffraction ring that is characteristic of a liquid, indicating that the region of the film from which the diffraction patterns were obtained has melted. Intensity in the {200} peak begins to return at ~20–25 ns. This broadening of the {111} diffraction feature ( $4.92 \text{ nm}^{-1}$ ) is shown in Figure 3c), which plots the full-width half-maximum (FWHM) of the {111} peak as a function of time. The FWHM values were obtained by subtracting the background from the radially averaged patterns and fitting the {111} peak to a Lorentzian profile. The initial FWHM of the {111} peak in the as-deposited film is  $0.36 \text{ nm}^{-1}$  and reaches a maximum of  $1.15 \text{ nm}^{-1}$  at 10 ns, after which it begins to decrease as the film re-solidifies. The diffraction data and analysis in Figure 3 indicate a liquid lifetime of ~20–25 ns.

To complement the dynamic TEM imaging of the pulsed-laser-induced self-assembly process, we simulated one-dimensional time-temperature profiles to mimic the spatial profile of the Gaussian laser beam and correlate to the experimentally observed temporal images and diffraction patterns. Briefly, the model is a one-dimensional finite element model and considers a 10-nm-thick nickel film on a 15-nm-thick silicon nitride membrane where the thermophysical properties of nickel and silicon nitride are considered and a melting temperature suppression of ~1676 K is assumed<sup>33,34</sup>. Zero absorption in the silicon nitride is assumed (only thermal conduction from the nickel film is included) and radiative heat loss is included, as thermal

conduction is ignored above and below the films due to the low pressure in the TEM. Figure 4 shows a series of time-temperature profiles as a function of radius (inset is the center region extended to longer times to illustrate the functionality of the radiative cooling). Considering the spatial and temporal variations due to the radial laser profile, there is good agreement between the experimentally determined ( $\sim 25\text{ns}+15\text{ns}$ ) and simulated liquid lifetimes of: center=50ns, 2  $\mu\text{m}$ =45ns, 4  $\mu\text{m}$ =36ns, 6  $\mu\text{m}$ =26ns, 8  $\mu\text{m}$ =11ns. From Figure 4, the simulated radius of the melted nickel film region is  $\sim 8\text{--}10 \mu\text{m}$ . The actual melt radius as demonstrated by the morphological changes in the 15- and 20-ns DTEM images in Figure 2 appears to be  $\sim 10\text{--}15 \mu\text{m}$ . This difference in the estimated and observed melt radius is attributed to radial thermal conductivity, which is ignored in the thermal model.

As can be seen in Figure 2b) and 2c), both the radial profile and the dynamic TEM images capture well the evolution of the dewetting self-assembly process, which is attributed to a spinodal thin-film instability<sup>35-38</sup>. Spinodal thin-film instabilities are initiated by surface wave perturbations and importantly have correlated time and length scales. Examination of the radial profiles in Figure 2b) and 2c) shows that at large radii, holes form with a correlated time and length scale from surface wave perturbations. Individual holes grow, merge with neighboring holes, and form pseudo-linear chains that can subsequently break down via Rayleigh-Plateau instabilities to form nanoparticle arrays with correlated length scales. In addition to the radial profiles in each image, comparison of the 15- and 20-ns images in Figure 2 nicely demonstrates the dynamics of the thermally induced assembly process. Figure 2b) reveals that after only 15 ns (+15-ns electron pulse width) the center  $\sim 5 \mu\text{m}$  of the laser-heated region of the film has already evolved into nanoparticles. Examination of Figure 2c) shows that the saturated nanoparticle region extends to  $\sim 10 \mu\text{m}$ ; however, the nanoparticle size and spacing is slightly coarsened. The change in the saturated nanoparticle timescale is likely due to changes in the time-temperature profiles as a function of radius and the resultant change in viscosity in the high-temperature center—the instability hole formation, hole growth, and Rayleigh-Plateau instability are all accelerated at lower viscosity. For instance, image analysis of a  $5 \mu\text{m} \times 5 \mu\text{m}$  box in the lower left corner of Figure 2d), which correlates to the near laser spot center and hottest region, reveals an average particle diameter of  $\sim 120 \text{nm}$  and from the fast Fourier transform of the area an average spacing of  $\sim 385 \text{nm}$ . If one examines a similar sized area beyond an  $\sim 10 \mu\text{m}$  radial

position, the average particle size is  $\sim 170$  nm and the spacing is  $\sim 670$  nm. While the particle size could be affected by some evaporative loss due to the higher cumulative thermal profile, the nanoparticle spacing is determined by the instability. Thus, based on the observed temporal imaging, we attribute the change in length scale to the change in the instability mechanism: namely, that the central  $\sim < 10$ - $\mu\text{m}$  region is driven by a spinodal liquid-phase instability and beyond the melted region, a solid-state dewetting process<sup>39-41</sup> that leads to a longer length scale is operative. The observed solid-state dewetting beyond the liquid melt region is unique to what has been typically observed on bulk substrates, which is likely due to radiative versus thermal conduction cooling. The inset in Figure 4 also shows for comparison the equivalent time-temperature profile of the center energy density of  $250 \text{ mJ/cm}^2$  for a 10-nm-thick nickel film on the 15-nm-thick nitride membrane and an energy density of  $325 \text{ mJ/cm}^2$  to reach a comparable peak temperature on a bulk (50- $\mu\text{m}$ -thick) silicon nitride substrate. Clearly the sample cooling is expedited on the bulk substrate due to thermal conduction and thus solid-state mechanisms typically not observed could be operative. Imaging at longer time scales will be investigated in the future to examine these solid-state mechanisms.

In summary, we have for the first time captured the nanoscale time and spatial dynamics of liquid-phase self-assembly of a 10-nm-thick nickel film suspended on a silicon nitride membrane into a nanoparticle array. The correlated time and length scales of the assembly process suggest that assembly is induced via a spinodal thin-film instability. Dynamic TEM imaging illustrates the spinodal dewetting evolution process and dynamic electron diffraction analysis confirms the metallic liquid lifetimes, determined to be  $\sim 25$  ns. Complementary finite-element modeling of the laser-irradiated films agrees well with the measured liquid lifetime and the observed radial profiles of the TEM images that are generated as a result of the Gaussian laser profile.

## Methods

Nickel films were dc magnetron sputter deposited directly onto 15-nm-thick silicon nitride TEM membranes (Ted Pella, Inc., Redding, CA). The nickel films were then exposed to a variety of fluences using a 1064-nm wavelength, 15-ns pulsed laser source with a Gaussian beam profile ( $1/e^2$  diameter of  $135 \pm 5 \mu\text{m}$ ), and an adequate melt threshold was observed using a total

deposited energy of  $\sim 4.1 \mu\text{J}$ . Subsequent to determining appropriate laser conditions for the nickel melting and self-assembly, the 10-nm-thick nickel films were laser-heated and *in-situ* observations of the dewetting process were conducted in the dynamic transmission electron microscope (DTEM) operating in both conventional TEM and pulsed-electron modes at 200 kV. The DTEM is a modified JEOL 2000FX TEM that incorporates two nanosecond pulsed lasers to drive both the specimen and a photocathode<sup>20</sup>, allowing pump-probe experiments with single-shot imaging and diffraction capabilities at high spatiotemporal resolution. Dynamic processes in the specimen are initiated with an  $\sim 15\text{-ns}$ -pulse-width neodymium-doped yttrium-aluminum-garnet (Nd:YAG) laser (1064 nm wavelength); a neodymium-doped yttrium-lithium-fluoride (Nd:YLF) laser that is frequency quintupled to 211 nm stimulates a photoemission electron source to generate  $>2 \times 10^9$  electrons in a 15-ns pulse. The time delay between the pump and probe laser pulses can be controlled from nanoseconds to hundreds of microseconds with a timing jitter of  $\pm 1$  ns. Further details on the configuration of the DTEM can be found in prior publications<sup>21,22,27</sup>.

The thermal model is a one-dimensional finite-element model based on the Fourier heat diffusion equation. The model uses a 1-nm spatial resolution spacing and a time step of 1 fs to capture both the thermal absorption of the laser energy and the temporal profile of the laser pulse. The simulation considers a 10-nm-thick nickel film on a 15-nm-thick silicon nitride membrane. To account for the incident angle of the laser beam (45 degrees) a thickness of 14 nm and 21 nm were used for the nickel film and silicon nitride membrane, respectively. The thermophysical properties of nickel and silicon nitride are considered and a melting temperature suppression of  $\sim 1676$  is assumed<sup>33,34</sup>. Zero absorption in the silicon nitride is assumed (only thermal conduction from the nickel film). Radiative heat loss is included at the top of the nickel film and the bottom of the silicon nitride membrane. Thermal conduction at the system boundaries is not considered due to the low pressure in the TEM.

#### Supporting Information

Figures S1 and S2. This material is available free of charge via the Internet at <http://pubs.acs.org>.

## Acknowledgements

J.D.F, P.D.R. acknowledge support from the U.S. Department of Energy, Basic Energy Sciences, Materials Sciences and Engineering Division for supporting the portions of this work related to understanding the liquid phase assembly dynamics and analysis. N.A.R. was supported by an ASEE/NSF fellowship. J.D.F, P.D.R., and N.A.R. also acknowledge that the nickel sputter deposition was conducted at the Center for Nanophase Materials Sciences, which is sponsored at Oak Ridge National Laboratory by the Office of Basic Energy Sciences, U.S. Department of Energy. Work at Lawrence Livermore National Laboratory was performed under the auspices of the U.S. Department of Energy, Office of Science, Office of Basic Energy Sciences, Division of Materials Sciences and Engineering under Contract DE-AC52-07NA27344.

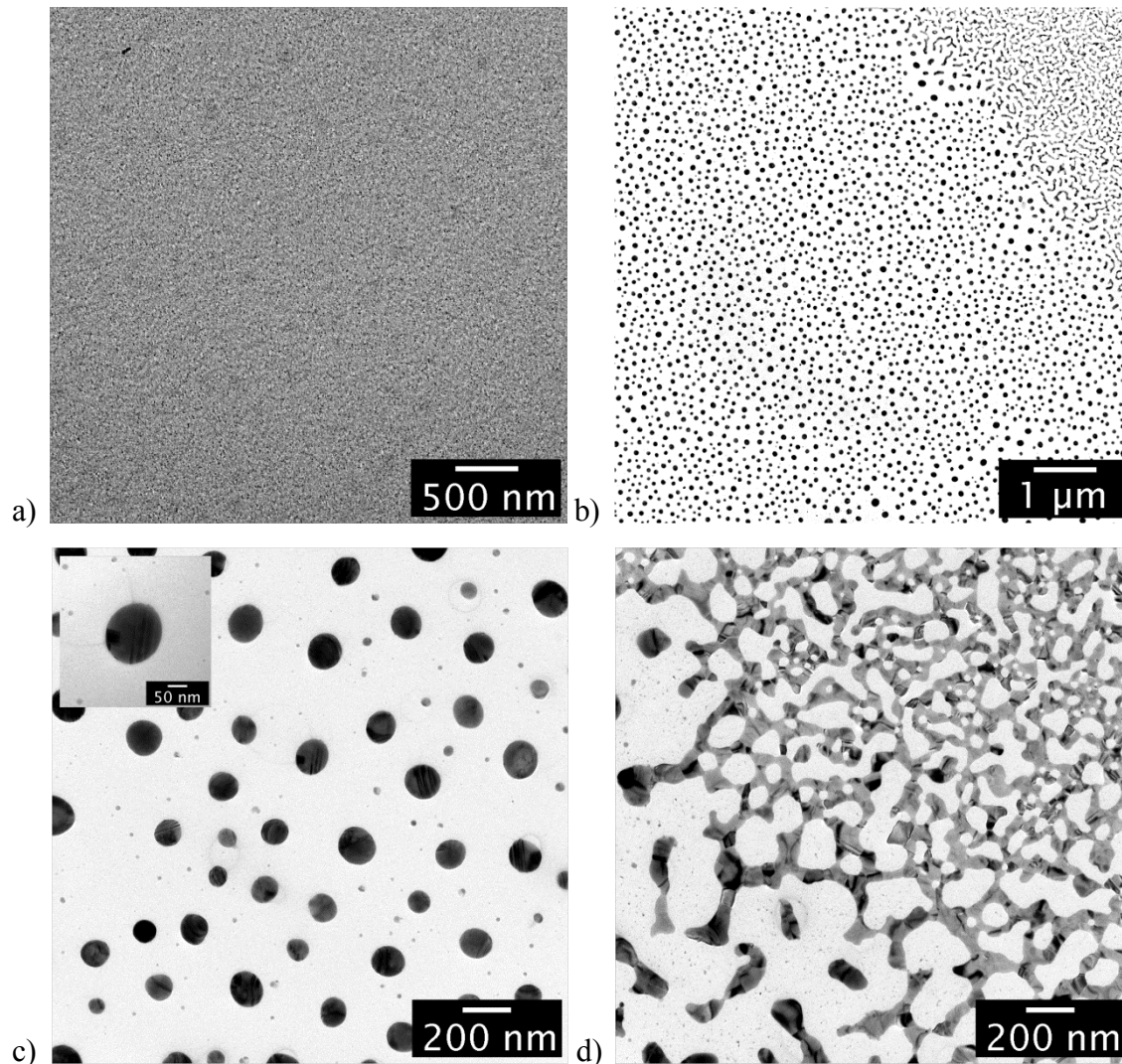
## References

1. Plateau, J. *Ann. Rep. Smithsonian Inst.* **1873**, 1863, 270-285.
2. Rayleigh, L. *Proc. London Math. Soc.* **1878**, 10, 4-13.
3. Herminghaus, S.; Jacobs, K.; Mecke, K.; Bischof, J.; Fery, A.; Ibn-Elhaj, M.; Schlagowski, S. *Science* **1998**, 282 (5390), 916-919.
4. Henley, S. J.; Carey, J. D.; Silva, S. R. P. *Phys. Rev. B* **2005**, 72 (19), 195408.
5. Trice, J.; Thomas, D.; Favazza, C.; Sureshkumar, R.; Kalyanaraman, R. *Phys. Rev. B* **2007**, 75 (23), 235439.
6. Trice, N.; Favazza, C.; Thomas, D.; Garcia, H.; Kalyanaraman, R.; Sureshkumar, R. *Phys. Rev. Lett.* **2008**, 101 (1), 017802.
7. Lin, C. H.; Jiang, L.; Zhou, J.; Xiao, H.; Chen, S. J.; Tsai, H. L. *Opt. Express* **2010**, 35 (7), 941-943.
8. Shirato, N.; Krishna, H.; Kalyanaraman, R. *J. Appl. Phys.* **2010**, 108 (2), 024313.
9. Wu, Y. Y.; Fowlkes, J. D.; Rack, P. D. *J. Mater. Res.* **2011**, 26 (2), 277-87.
10. Fowlkes, J. D.; Kondic, L.; Diez, J. A.; Wu, Y. Y.; Rack, P. D. *Nano Lett.* **2011**, 11 (6), 2478-2485.
11. Kondic, L.; Diez, J. A.; Rack, P. D.; Guan, Y. F.; Fowlkes, J. D. *Phys. Rev. E* **2009**, 79 (2), 026302.
12. Wu, Y. Y.; Fowlkes, J. D.; Rack, P. D.; Diez, J. A.; Kondic, L. *Langmuir* **2010**, 26 (14), 11972-11979.
13. Wu, Y. Y.; Fowlkes, J. D.; Roberts, N. A.; Diez, J. A.; Kondic, L.; Gonzalez, A. G.; Rack, P. D. *Langmuir* **2011**, 27 (21), 13314-13323.
14. Guan, Y. F.; Pearce, R. C.; Melechko, A. V.; Hensley, D. K.; Simpson, M. L.; Rack, P. D. *Nanotechnology* **2008**, 19 (23), 235604.
15. Rack, P. D.; Guan, Y.; Fowlkes, J. D.; Melechko, A. V.; Simpson, M. L. *Appl. Phys. Lett.* **2008**, 92 (22), 223108.
16. Habenicht, A.; Olapinski, M.; Burmeister, F.; Leiderer, P.; Boneberg, J. *Science* **2005**, 309 (5743), 2043-2045.
17. Fuentes-Cabrera, M.; Rhodes, B. H.; Baskes, M. I.; Terrones, H.; Fowlkes, J. D.; Simpson, M. L.; Rack, P. D. *ACS Nano* **2011**, 5 (9), 7130-7136.

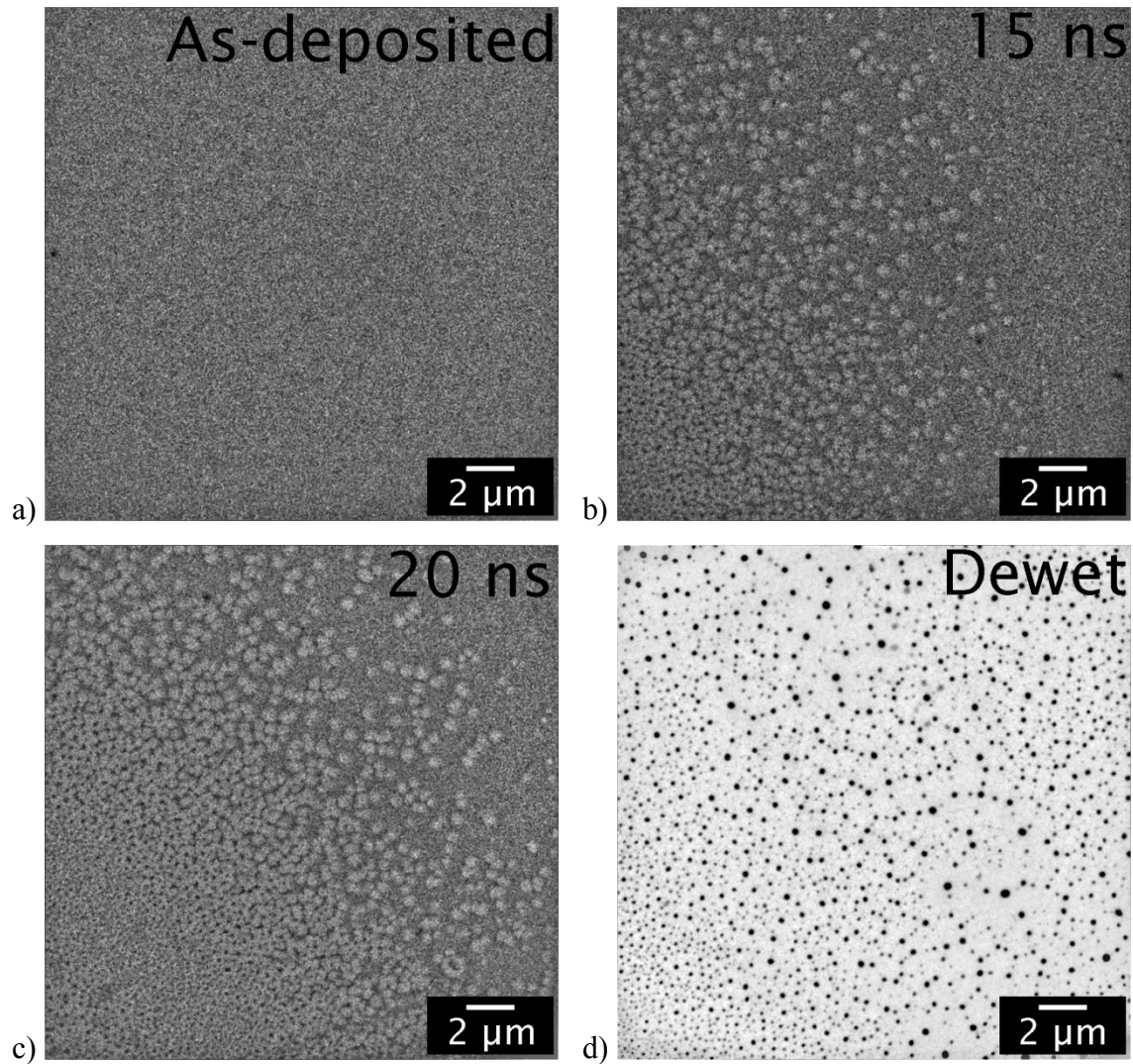
18. Fuentes-Cabrera, M.; Rhodes, B. H.; Fowlkes, J. D.; Lopez-Benzanilla, A.; Terrones, H.; Simpson, M. L.; Rack, P. D. *Phys. Rev. E* **2011**, 83 (4), 041603.
19. Favazza, C.; Kalyanaraman, R.; Sureshkumar, R. *J. Appl. Phys.* **2007**, 102 (10), 104308.
20. King, W. E.; Campbell, G. H.; Frank, A.; Reed, B.; Schmerge, J. F.; Siwick, B. J.; Stuart, B. C.; Weber, P. M. *J. Appl. Phys.* **2005**, 97 (11), 111101.
21. LaGrange, T.; Armstrong, M. R.; Boyden, K.; Brown, C. G.; Campbell, G. H.; Colvin, J. D.; DeHope, W. J.; Frank, A. M.; Gibson, D. J.; Hartemann, F. V.; Kim, J. S.; King, W. E.; Pyke, B. J.; Reed, B. W.; Shirk, M. D.; Shuttlesworth, R. M.; Stuart, B. C.; Torralva, B. R.; Browning, N. D. *Appl. Phys. Lett.* **2006**, 89 (4), 044105.
22. Kim, J. S.; LaGrange, T.; Reed, B. W.; Taheri, M. L.; Armstrong, M. R.; King, W. E.; Browning, N. D.; Campbell, G. H. *Science* **2008**, 321 (5895), 1472-1475.
23. LaGrange, T.; Campbell, G. H.; Reed, B.; Taheri, M.; Pesavento, J. B.; Kim, J. S.; Browning, N. D. *Ultramicroscopy* **2008**, 108 (11), 1441-1449.
24. Reed, B. W.; Armstrong, M. R.; Browning, N. D.; Campbell, G. H.; Evans, J. E.; LaGrange, T.; Masiel, D. J. *Microsc. Microanal.* **2009**, 15 (4), 272-281.
25. Browning, N. D.; Campbell, G. H.; Hawreliak, J. A.; Kirk, M. A. *MRS Bull.* **2010**, 35 (12), 1009-1016.
26. Campbell, G. H.; LaGrange, T.; Kim, J. S.; Reed, B. W.; Browning, N. D. *J. Electron Microsc.* **2010**, 59, S67-S74.
27. Reed, B. W.; LaGrange, T.; Shuttlesworth, R. M.; Gibson, D. J.; Campbell, G. H.; Browning, N. D. *Rev. Sci. Instrum.* **2010**, 81 (5), 053706.
28. Samsonov, G. V.; Panasyuk, A. D.; Finkel'shtein, I. M. *Powder Metall. Met. Ceram.* **1977**, 16 (5), 392-394.
29. Alfonso, J. A.; Greaves, E. D.; Lavelle, B.; Sajo-Bohus, L. *J. Vac. Sci. Technol. A* **2003**, 21 (4), 846-850.
30. Fowlkes, J. D.; Melechko, A. V.; Klein, K. L.; Rack, P. D.; Smith, D. A.; Hensley, D. K.; Doktycz, M. J.; Simpson, M. L. *Carbon* **2006**, 44 (8), 1503-1510.
31. Randolph, S. J.; Fowlkes, J. D.; Melechko, A. V.; Klein, K. L.; Meyer, H. M.; Simpson, M. L.; Rack, P. D. *Nanotechnology* **2007**, 18 (46), 465304.
32. Siwick, B. J.; Dwyer, J. R.; Jordan, R. E.; Miller, R. J. D. *Science* **2003**, 302 (5649), 1382-1385.

33. Bassler, B. T.; Hofmeister, W. H.; Carro, G.; Bayuzick, R. J. *Metall. Mater. Trans. A* **1994**, 25 (6), 1301-1308.
34. Zhang, Z.; Li, J. C.; Jiang, Q. *J. Phys. D. Appl. Phys.* **2000**, 33 (20), 2653-2656.
35. Reiter, G.; Sharma, A.; Casoli, A.; David, M. O.; Khanna, R.; Auroy, P. *Langmuir* **1999**, 15 (7), 2551-2558.
36. Seemann, R.; Herminghaus, S.; Jacobs, K. *J. Phys. Condens. Matter* **2001**, 13 (21), 4925-4938.
37. Seemann, R.; Herminghaus, S.; Jacobs, K. *Phys. Rev. Lett.* **2001**, 86 (24), 5534-5537.
38. Xie, R.; Karim, A.; Douglas, J. F.; Han, C. C.; Weiss, R. A. *Phys. Rev. Lett.* **1998**, 81 (6), 1251-1254.
39. Mullins, W. W. *J. Appl. Phys.* **1957**, 28 (3), 333-339.
40. Mullins, W. W. *J. Appl. Phys.* **1959**, 30 (1), 77-83.
41. Nichols, F. A.; Mullins, W. W. *Trans. Metall. Soc. AIME* **1965**, 233 (10), 1840-1847.

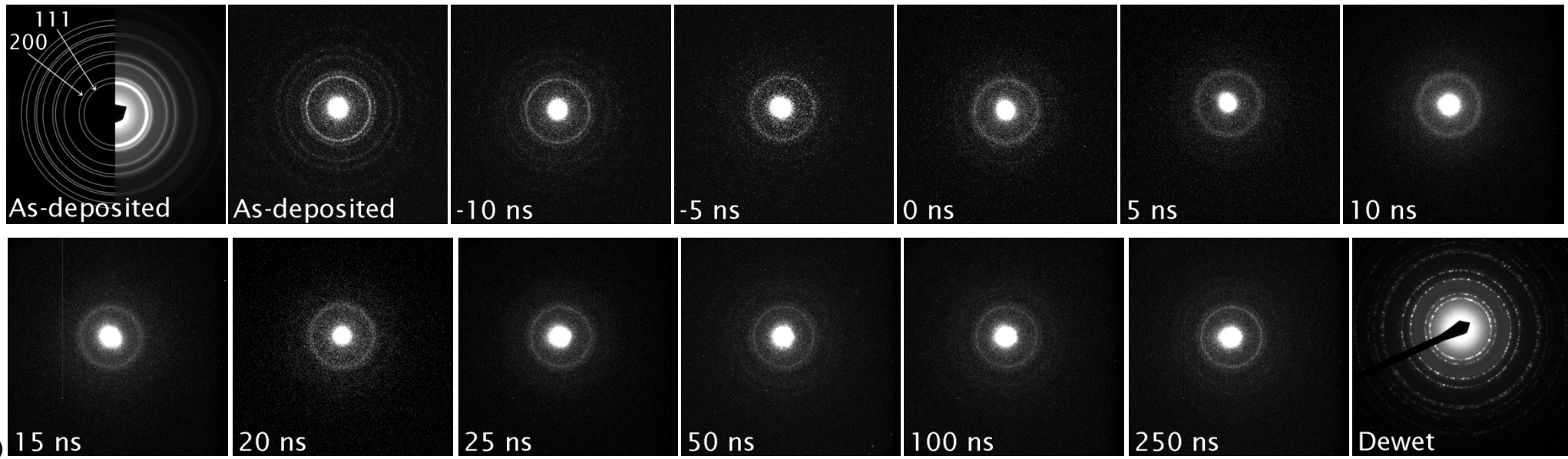
## Figures

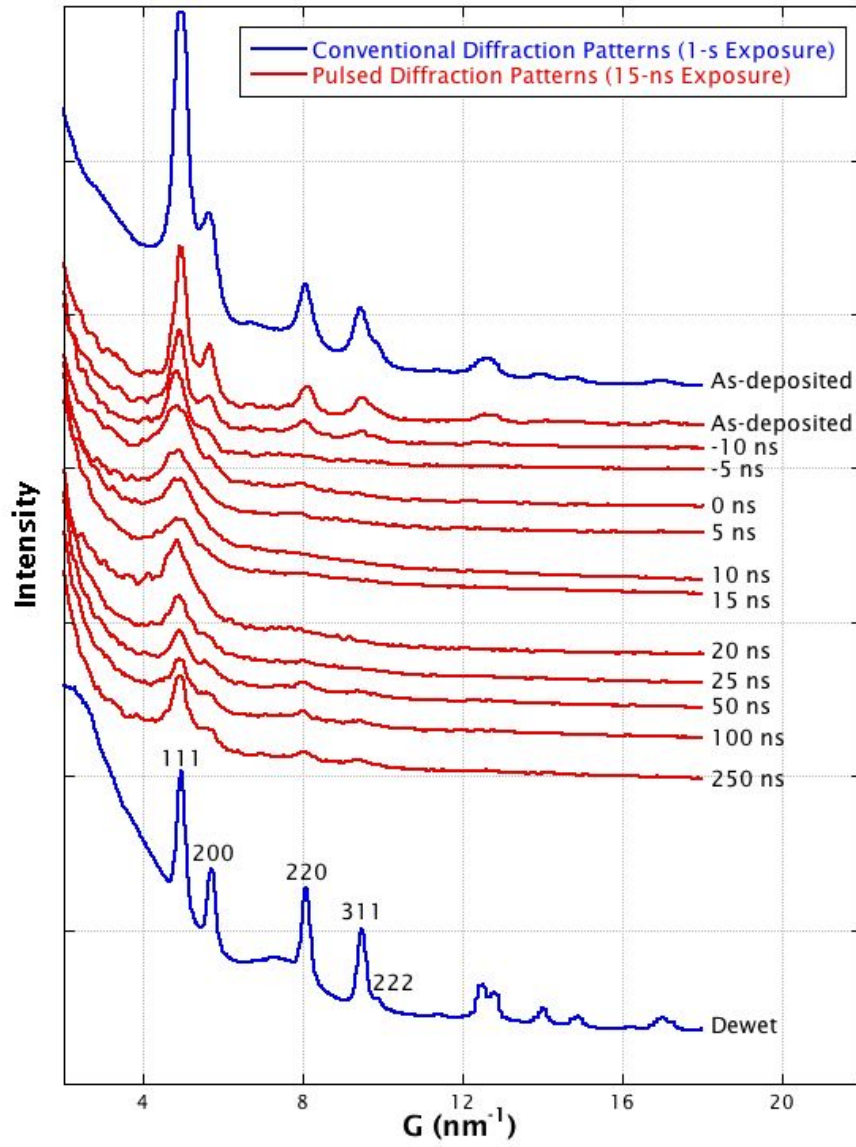


**Figure 1:** Conventional bright-field TEM images of a) the as-deposited Ni film and b) the Ni film after pulsed-laser-induced dewetting. The image of the dewet film was recorded near the edge of the laser spot (the center of the laser spot is not shown, but was in the direction of the lower-left corner of the image) to illustrate the effect of the Gaussian laser profile on the final morphology. Higher-magnification images of both dewet morphologies are shown in c) and d). Inset in (c) shows twinning in a nanoparticle, consistent with rapid solidification.

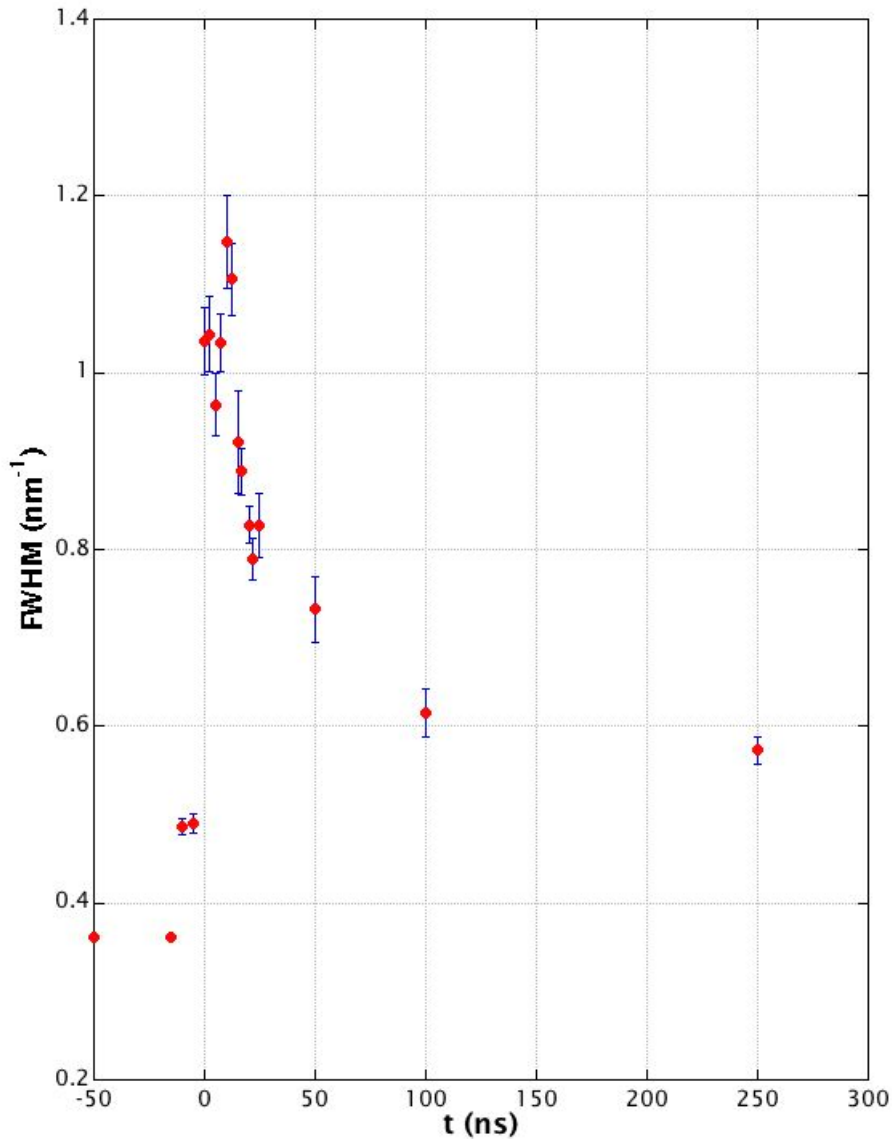


**Figure 2:** Time-resolved (15-ns exposure times) images of the a) as-deposited Ni film, b,c) the film as it dewets the substrate at time delays of b) 15 ns and c) 20 ns, and d) the dewet film, recorded ~30 s after the laser pulse. The center of the laser pulse was toward the lower-left corner of the images.





b)



c)

**Figure 3:** a) Diffraction patterns showing the time evolution of the film as it dewets the substrate. The initial diffraction pattern recorded from the as-deposited film shows the simulated Ni diffraction pattern overlaid on the experimental pattern, recorded with a 1-s exposure time. The time evolution was followed in 5-ns intervals using 15-ns exposure times. b) Radially averaged intensity as a function of reciprocal lattice vector for all diffraction patterns shown in a). c) A plot of the full-width half-maximum (FWHM) of the peak centered around the {111} peak position ( $4.92 \text{ nm}^{-1}$ ) as a function of time.

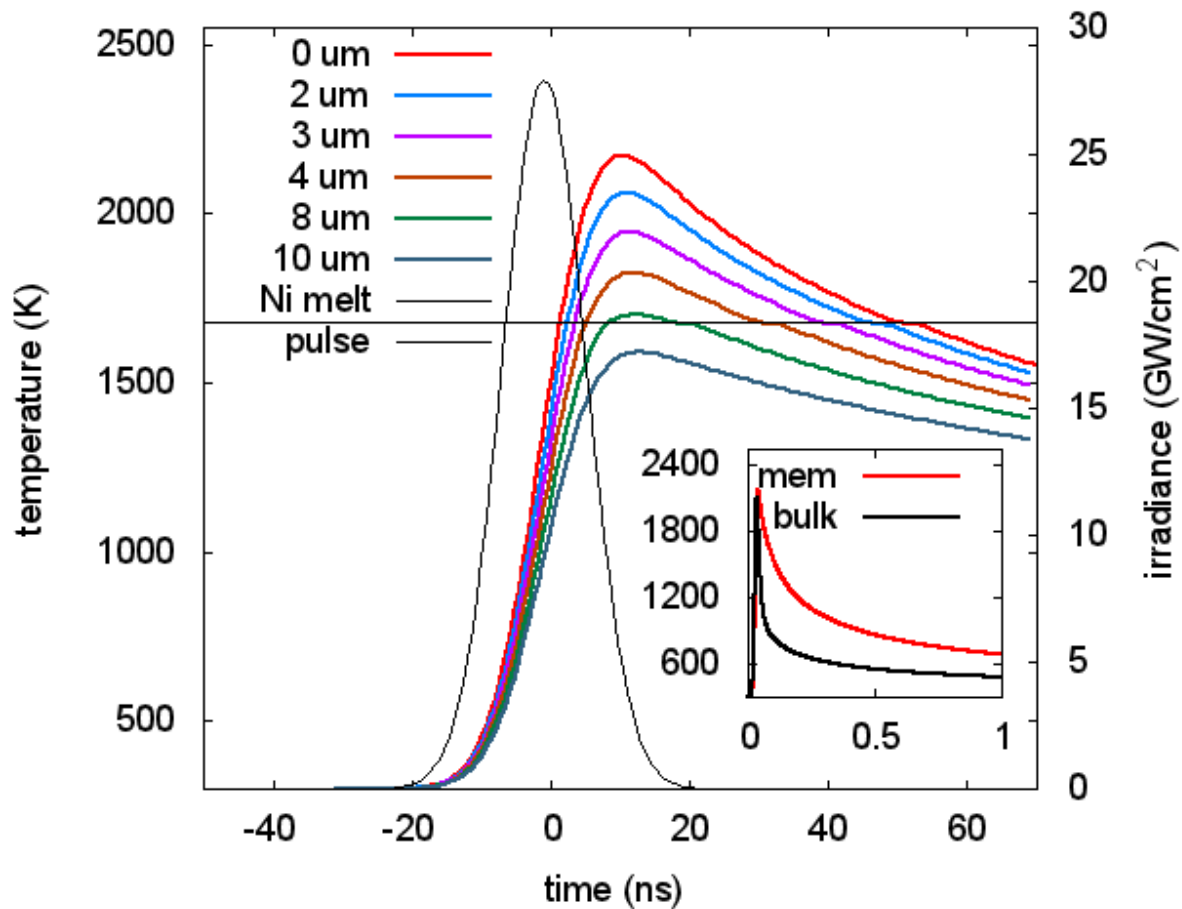


**Figure 4:** Simulated nickel time-temperature profiles as a function of the Gaussian laser radius, demonstrating an approximately 8- $\mu\text{m}$  melt radius. Inset compares the nickel time-temperature profiles (to 1  $\mu\text{s}$ ) of the peak energy density ( $250 \text{ mJ}/\text{cm}^2$ ) on the thin membrane versus a larger laser energy density ( $325 \text{ mJ}/\text{cm}^2$ ) on a bulk silicon nitride sample. The more rapid cooling associated with thermal conduction on the bulk substrate is clear relative to the radiative cooling that dominates the nickel on the silicon nitride membrane.

Supporting Information

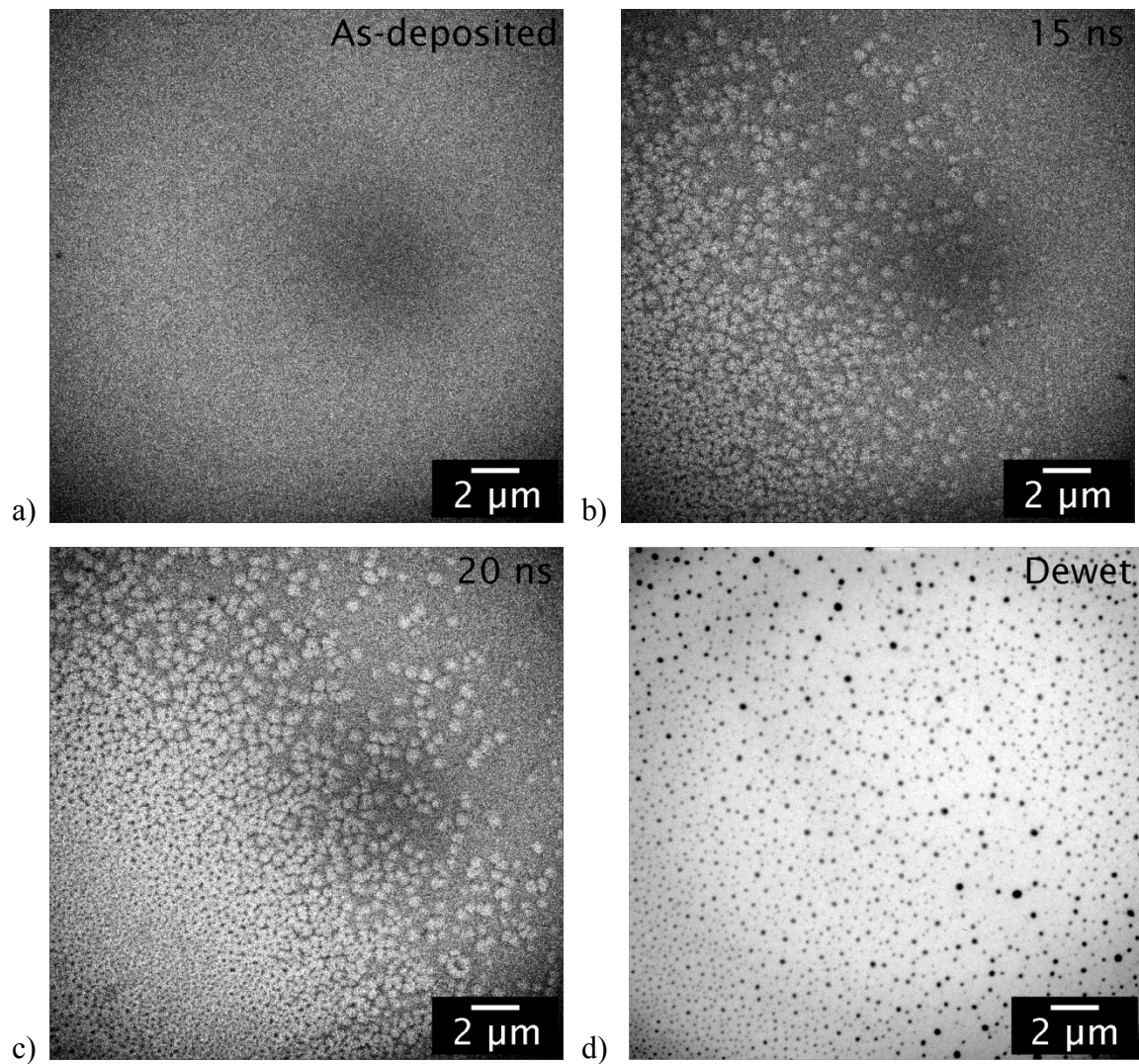


**Figure S1:** Raw time-resolved images of the a) as-deposited Ni film, b,c) the film as it dewets the substrate at time delays of b) 15 ns and c) 20 ns, and d) the dewet film, recorded ~30 s after the laser pulse. Images are the same as Figure 2, but without filtering.

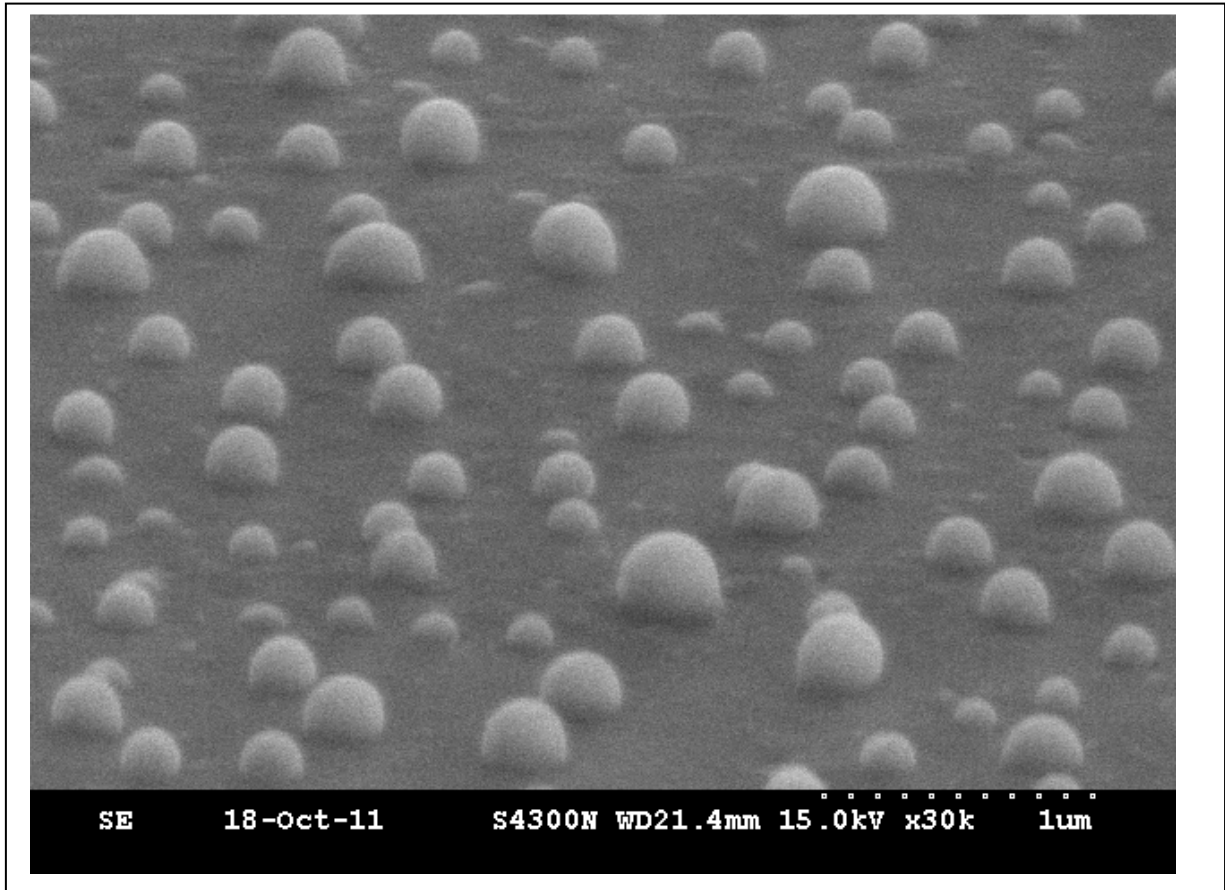


**Figure S2:** Tilted scanning electron micrograph of a 10-nm-thick nickel film deposited on a 100-nm-thick silicon nitride thin film on a silicon substrate. The film was pulsed-laser treated to measure the liquid nickel–silicon nitride wetting angle.